

# Breakup of a surfactant-laden drop in a continuous air jet stream

Sumit Joshi, Sushrut Ranade, T.N.C. Anand\*

Department of Mechanical Engineering, Indian Institute of Technology Madras, Chennai  
600036, India

\*Corresponding author: [anand@iitm.ac.in](mailto:anand@iitm.ac.in)

## Abstract

In this study, we investigate the breakup behaviour of a surfactant-laden drop in a continuous air jet stream. A solution of sodium lauryl sulfate (SLS) in water was used as a test liquid. The range of Weber numbers employed was 19.8–72.4. We observed bag breakup, bag-stamen breakup, dual-bag breakup and sheet-thinning breakup. A few important parameters such as stream-wise length and cross-stream length of the drop, the time at which the first instance of breakup is observed, and the displacement of the drop centroid were measured. Two approaches to obtain the velocity and acceleration of the drop from the centroid displacement data are discussed: central difference approximations and polynomial fitting using the ridge regression. Finally, the coefficient of drag of the drop at different Weber numbers, calculated using the velocity and acceleration data (obtained by employing both the approaches), is compared.

## Keywords

Surfactant-laden drop, drop breakup, Weber number, coefficient of drag.

## Introduction

Drop breakup/secondary breakup occurs in a wide variety of natural and human-made phenomena. It plays an important role in finalizing a drop size distribution which is one of the most important parameters in a spray. The objective of most of the atomization processes is to control the final drop size distribution. Studying drop breakup may help in optimizing the process parameters for obtaining the desired drop size distribution [5]. Therefore, this field has received great attention from researchers over the years.

When the drop encounters a flow-field at a different velocity than itself, aerodynamic force tries to deform it, while surface tension and viscous forces resist the deformation, and hence breakup. Weber number is defined as the ratio of the disrupting aerodynamic force to the restorative surface tension force as,

$$We = \frac{\rho_a U^2 d_0}{\sigma}, \quad (1)$$

where  $\rho_a$  is the gas density (air density in most cases),  $U$  is the initial relative velocity between the drop and the gas,  $d_0$  is the undeformed drop diameter, and  $\sigma$  is surface tension. Ohnesorge number represents the ratio of the liquid viscous force to the surface tension and inertial forces as,

$$Oh = \frac{\mu_l}{\sqrt{\rho_l d_0 \sigma}}, \quad (2)$$

where  $\mu_l$  is the liquid viscosity, and  $\rho_l$  is the liquid density. When  $Oh < 0.1$ , viscous effects can be neglected [6], and Weber number is the controlling parameter [14] (in this study,  $Oh < 0.1$ ). As the Weber number increases, modes of breakup change from no breakup/vibrational breakup, bag breakup, multimode breakup (bag-stamen breakup), sheet-thinning breakup to catastrophic breakup [5]. There exist other non-dimensional numbers such as Reynolds number ( $Re = \rho_a U d_0 / \mu_a$  where  $\mu_a$  is air viscosity), viscosity ratio ( $N = \mu_l / \mu_a$ ) and density ratio ( $\epsilon = \rho_l / \rho_a$ ). However, most of the times,  $We$  and  $Oh$  suffice to characterize breakup phenomenon largely [6, 10].

A surfactant, when added to a liquid, reduces its surface tension. The variation in surface tension of a surfactant-laden liquid depends on the amount of surfactant added to it. As mentioned before, the lesser the surface tension, the lesser is the resistance to deformation, and easier is the breakup. Hence, surfactant solutions are used in engineering applications such as crop spraying, inkjet printing and cleaning sprays to control drop breakup by controlling the amount of surfactant used [18, 19]. Applications, where other aspects of the surfactant-laden liquid (such as its enhanced spreadability) are more important than its ease in spraying, are coating processes (food processing, medicines), and materials processing [9].

Zhao *et al.* [18, 19] investigated breakup of surfactant-laden drops. Both these studies discuss mostly the bag breakup mode. However, in this study, along with the bag breakup mode, we also discuss bag-stamen breakup, dual-bag breakup and sheet-thinning breakup modes. We employed a solution of water and sodium lauryl sulfate (water-SLS solution, 0.18 wt%) as a test liquid (the surfactant concentration is close to a critical micelle concentration (CMC) [15]). The primary objective of the present work is to provide experimental results for the mean breakup behaviour of the surfactant-laden drop in different breakup modes.

### Experimental methods

The experimental setup consisted of four systems as follows: (1) a drop generation system, (2) an air flow system, (3) a photographic system, and (4) a drop detection system.

The drop generation system consisted of a stainless steel needle (with an internal diameter of  $180\ \mu\text{m}$ ) connected to a syringe pump (Fig. 1), which was operated at a constant flow rate to achieve repeatable generation of drops. Drops fell under gravity. The maximum falling velocity (y-velocity) of the drop in the present experiments was found to be around 2 m/s.

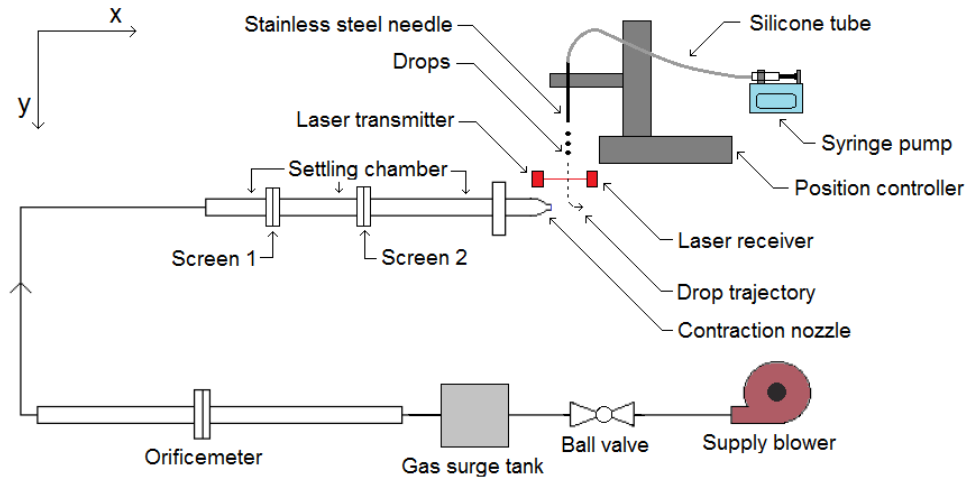


Figure 1. Schematic of the experimental apparatus.

We employed a continuous jet method as in [1, 4] (Fig. 1). In our experiments, the air flow system generated a continuous air jet. The system consisted of a supply blower, a ball valve (to regulate the flow rate), a gas surge tank (to dampen flow rate fluctuations), an orificemeter, a settling chamber with screens (to reduce turbulence and increase uniformity of the flow), and a contraction nozzle. A Laser Doppler Velocimeter was used to measure the velocity profile of the air jet coming out of the contraction nozzle at a distance of 5 mm from nozzle exit. Figure 2 shows the mean and r.m.s. component of the velocity (x-velocity) of the air jet in a direction parallel to the axis of the nozzle.

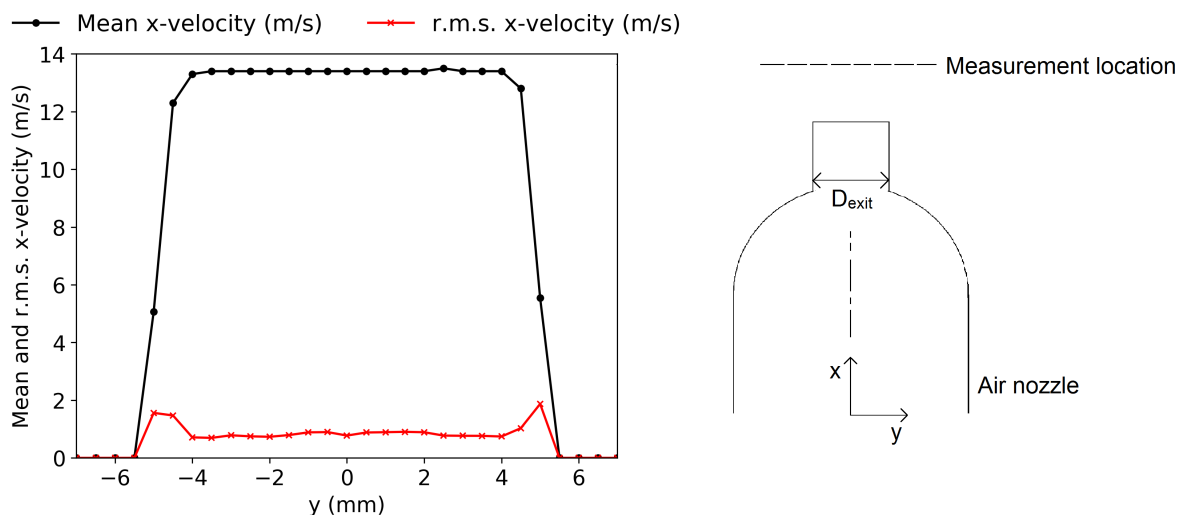


Figure 2. Mean and r.m.s. air velocities in the x-direction at a distance of 5 mm from the nozzle exit. The schematic of the air nozzle and the coordinate system used for the measurement of the velocity profile are also shown.

The photographic system consisted of a high-speed camera, a lens of focal length 105 mm, a halogen lamp as a light source (500 W) and a light diffuser. Images were captured through a backlit shadow imaging technique. The frame rate was 8000 Hz, and the magnification was  $32.3\ \mu\text{m}$  per pixel.

To save time while imaging a large number of drops, and repeat the experiment several times, a drop detection system consisting of a laser transmitter and a receiver (source: Robokits India) was employed (Fig. 1). Both of

**Table 1.** Properties of the solution of water and sodium lauryl sulfate (water-SLS solution, 0.18 wt%).

Liquid	$\sigma$ (N/m)	$\mu_l$ (Pa·s)	$\rho_l$ (kg/m <sup>3</sup> )
Water-SLS solution (0.18 wt%)	0.0317 (25 °C)	$8.6 \times 10^{-4}$ (25 °C)	999

**Table 2.** Summary of the test conditions. (The uncertainty in the Weber number is calculated from the uncertainty in  $U$  and  $d_0$  only, as the uncertainties in  $\rho_a$  and  $\sigma$  are negligibly small.  $\rho_a = 1.2$  kg/m<sup>3</sup>.)

$We$	Uncertainty in $We$	$U$ (m/s)	$d_0$ (m/s)	$Oh$	$Re$
19.8	$\pm 0.6$	18.3	1.56	$3.9 \times 10^{-3}$	1855
26.4	$\pm 0.2$	21.1	1.56	$3.9 \times 10^{-3}$	2140
33.9	$\pm 0.1$	24	1.55	$3.9 \times 10^{-3}$	2418
49.5	$\pm 0.8$	28.9	1.56	$3.9 \times 10^{-3}$	2930
58.8	$\pm 1.1$	31.8	1.54	$3.9 \times 10^{-3}$	3173
72.4	$\pm 1.4$	35.1	1.55	$3.9 \times 10^{-3}$	3531

them were powered by an Arduino Uno board. The Arduino Uno board triggered the camera once it detected a change in the voltage level of the laser receiver, caused by the drop cutting the laser beam. The high-speed camera recorded a pre-set number of images which was sufficient to capture the important features of the breakup process in different breakup modes.

Table 1 and 2 show important liquid properties and the experimental conditions, respectively. The experiments were carried out within a day of the preparation of the solution. At least 100 drops were tested at each Weber number.

## Results and discussion

Figure 3 shows different breakup modes observed in the present experiments. As the Weber number increased, the breakup modes appeared in the following order: bag breakup, bag-stamen breakup, dual-bag breakup, and sheet-thinning breakup. Topological features of the drop (such as the presence of a bag/bags, a toroidal rim, nodes on the toroidal rim, a central stamen-like structure), and their length and time scales change significantly from one mode of breakup to another. Initial deformation of the drop into a disk-like structure seems to be a common characteristic of the breakup modes.

As Weber number increases, the central stamen-like structure appears along with a bag/bags (Fig. 3 (B, C, D)). It is connected to the rear end of the bag. However, this connection is different at different Weber numbers (Fig. 3 (B - e, C - e, D - d)). At  $We = 49.5$  (dual-bag breakup), the stamen is connected to multiple bags through thick filaments (Fig. 3 (D - d)). With the increase in Weber number, the thickness of the stamen increases, concentrating more mass inside it. This increases its inertia. Hence, the stamen moves slowly in the stream-wise direction compared to the bag (the bag travels faster in the flow because there is little mass in the bag, imparting it less inertia (Fig. 3 (C - e))). The slower moving stamen pulls on the portion where it connects to the bag (Fig. 3 (C - e)). This phenomenon may be happening intensively in the case of dual-bag breakup mode as the mass of the stamen is more, which imparts more inertia to it, and slows it down further. This, along with some form of instability on the stamen, could be some of the reasons we observed multiple bags (three, most of the times) in the dual-bag breakup mode (Fig. 3 (D - d)). The stamen is called a 'core drop' in the dual-bag breakup mode. This core drop breaks in the bag breakup mode (Fig. 3 (D - h)). The core drop in the case of the sheet-thinning breakup mode is not stretched in the stream-wise direction as in the case of bag-stamen and dual-bag breakup modes. In this mode, liquid sheets are stripped off the equator of the core drop (Fig. 3 (E - c)). The core drop breaks into a multitude of smaller droplets through multiple bag breakups.

We measured the following parameters of the drop: (1) stream-wise length ( $L$ ) and cross-stream length ( $2R$ ) (Fig. 3 (C - a)) till the first instance of breakup is observed (Fig. 3 (A - e)), (2) the time at which the first instance of breakup is observed (Fig. 3 (A - e), (B - e), (C - e), (D - d), (E - c)) (we call this time as the 'first rupture time'), and (3) displacement of the drop centroid. The stream-wise length ( $L$ ) and cross-stream length ( $2R$ ) were made non-dimensional by the undeformed drop diameter,  $d_0$  (Fig. 3 (B - a)). From the displacement of the drop centroid, the drop velocity and acceleration were calculated using two different methods which are discussed later. The velocity and acceleration data were used to calculate a coefficient of drag ( $C_d$ ) of the drop. The non-dimensional parameters,  $L/d_0$ ,  $2R/d_0$  and  $C_d$  were plotted versus non-dimensional time,  $t/t^*$ , where  $t^*$  is the characteristic secondary breakup time [12] expressed as,

$$t^* = \frac{d_0}{U} \sqrt{\frac{\rho_l}{\rho_a}}. \quad (3)$$

Figure 4 shows the variation of the parameters,  $2R/d_0$  and  $L/d_0$ , with  $t/t^*$  till the first rupture time for  $We = 19.8 - 72.4$ .

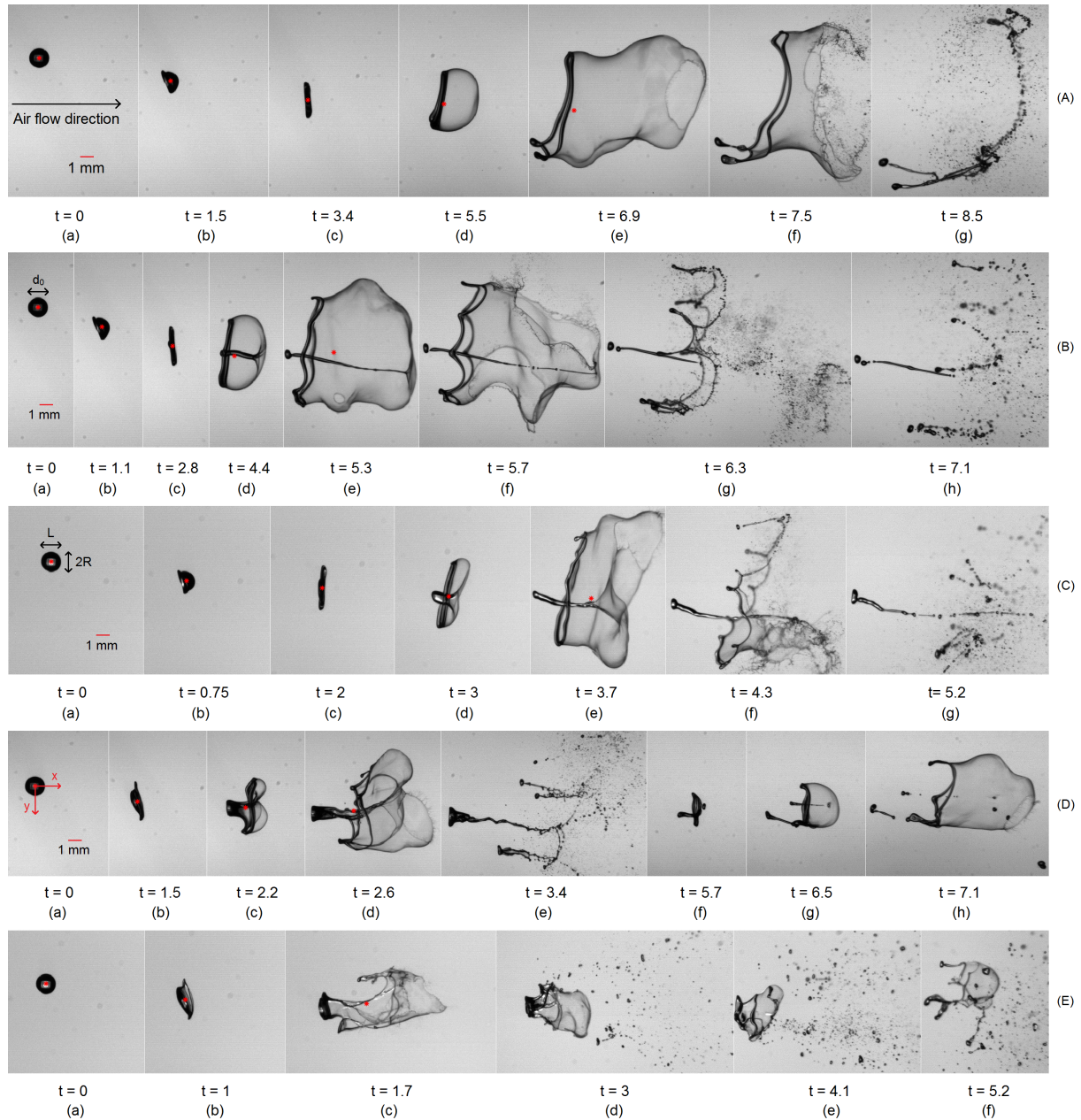


**Figure 3.** (A) Bag breakup ( $We = 19.8$ ), (B) bag-stamen breakup ( $We = 26.4$ ), (C) bag-stamen breakup ( $We = 33.9$ ) (D) dual-bag breakup ( $We = 49.5$ ), (E) sheet-thinning breakup ( $We = 72.4$ ). time ( $t$ ) is in milliseconds. The asterisk markers indicate the location of the centroids in different breakup modes.

Standard error, which is the ratio of standard deviation and square root of number of realizations ( $S/\sqrt{N}$ ), was used to represent the error bars. The rate of increase of  $2R/d_0$  increases slightly with the Weber number (Fig. 4 (A)). The plot of  $L/d_0$  versus  $t/t^*$  gives us an important parameter known as ‘initiation time’. At the initiation time,  $L/d_0$  achieves a minimum value, and the drop attains a disk-like shape [4]. The initial deformation of the drop into the disk-like structure in all the breakup modes is apparent in Fig. 3. Figure 5 shows that the first rupture time decreases with Weber number. It would be interesting to see if the total breakup time (the time after which no further breakup is observed [13]) shows a similar trend.

The displacement of the drop centroid in the x- and y-direction ( $x_c$  and  $y_c$ ) was measured till the first rupture time and plotted against time. The origin of the coordinate system used for this measurement is the centroid of the drop about to enter the cross-flow (Fig. 3 (D - a)). Figure 6 shows the variation of the x- and y-displacement of the drop centroid with time at all the Weber numbers in the present experiments. The x-displacement seems to be a strong function of  $We$  compared to the y-displacement. The y-displacement varies almost linearly with time at all the Weber numbers. After the initiation time, the centroid may not represent the actual center of mass of the drop in all the cases (Fig. 3 (E - c)). Hence, displacement data of the drop centroid may not be reliable after the initiation time.

From the x- and y-displacement versus time data of the drop centroid, we calculated the drop velocity and acceler-

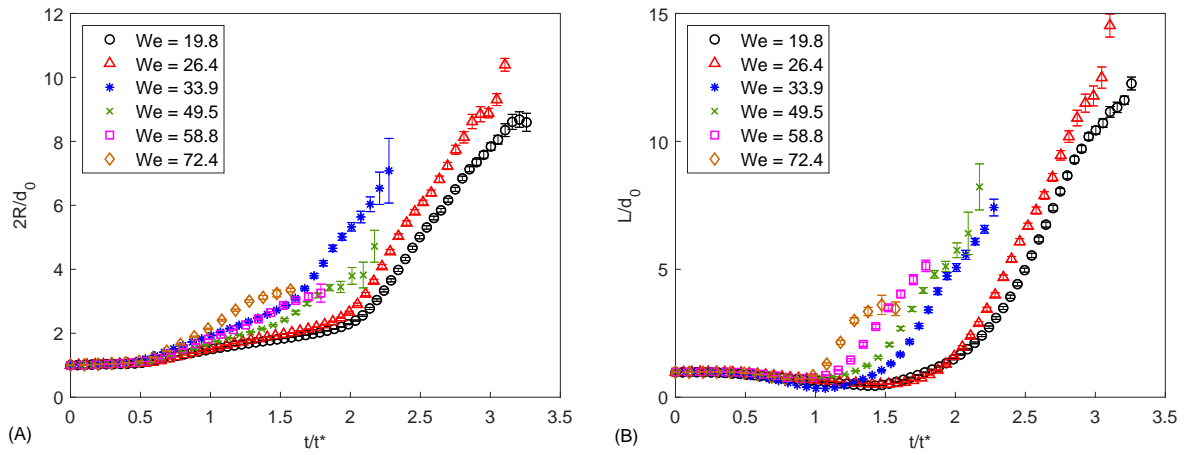


**Figure 4.** Variation of (A)  $2R/d_0$  and (B)  $L/d_0$  with  $t/t^*$  till the first rupture time in the present experiments.

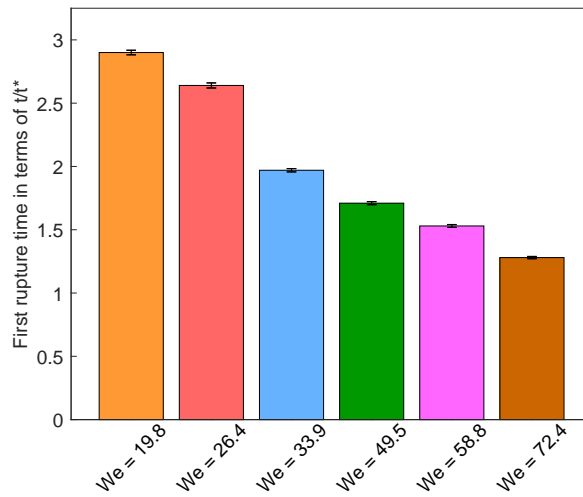


**Figure 5.** Variation of the first rupture time with the Weber numbers in the present experiments.

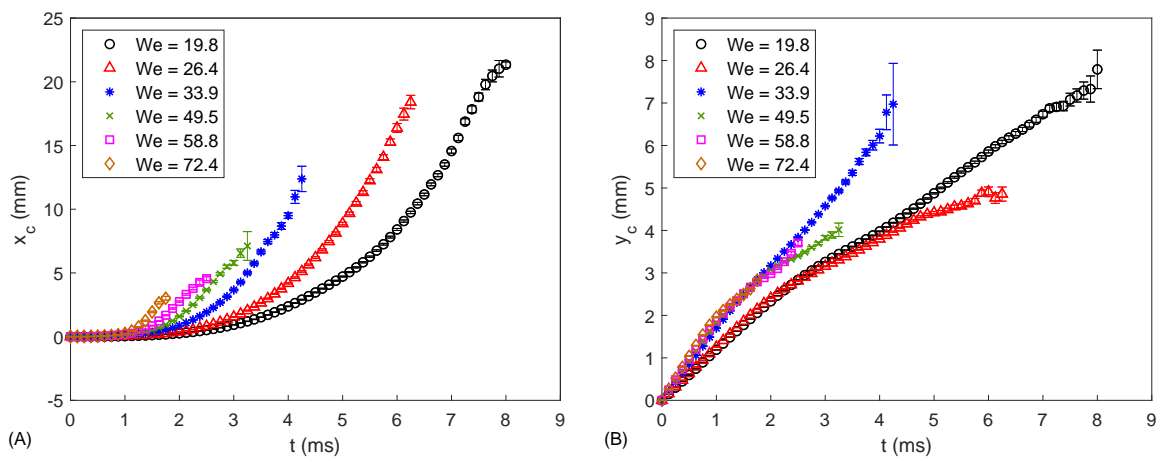


**Figure 6.** Variation of the drop centroid displacement in (A) x-direction ( $x_c$ ) and, (B) y-direction ( $y_c$ ) with time in the present experiments.

ation using two methods: central difference formula of  $2^{nd}$  order and polynomial fitting using the ridge regression.

A central difference formula of 4<sup>th</sup> order was also tried. However, we did not find a significant difference in the outcome compared to that of 2<sup>nd</sup> order.

For fitting polynomials to the x- and y-displacement versus time data of the drop centroid, we employed the ridge regression as it works better compared to the regular least squares method because of the bias-variance trade-off [8]. In the least squares method, the regression coefficients ( $\beta_0, \beta_1, \beta_2, \dots, \beta_p$ ) are determined by minimizing the sum of squared residuals ( $RSS$ ). The expression for  $RSS$  [8] is shown below,

$$RSS = \sum_{i=1}^n \left( y_i - \beta_0 - \sum_{j=1}^p \beta_j x_{ij} \right)^2, \quad (4)$$

where  $n$  is the total number of data points,  $y$  is the measured quantity/dependent variable/observation and  $x$  is the independent variable. In the ridge regression, the regression coefficients are determined by minimizing the following quantity,

$$RSS + \lambda \sum_{j=1}^p \beta_j^2, \quad (5)$$

where  $\lambda (\geq 0)$  is a tuning parameter. The term,  $\lambda \sum_j \beta_j^2$  is called as the shrinkage penalty [8]. For different values of  $\lambda$ , we get different regression coefficients. Before deciding the optimum value of  $\lambda$  (which is used to find the best-fit polynomial), we need to decide the optimum degree of the polynomial for the plots in Fig. 6. For that, the value of  $\lambda$  and the degree of the polynomial were varied in the ranges 0.001–100 and 1–8, respectively. We found that the polynomials with degrees 3 and 1, respectively, fit the x- and y- displacement versus time data. The above exercise avoids overfitting [8]. The optimum value of  $\lambda$  was calculated using one of the well-known resampling methods, Leave-One-Out Cross-Validation (LOOCV) [8].

Once the polynomials for the x- and y-displacement versus time data of the drop centroid (Fig. 6) are determined, the drop velocity and acceleration in the x- and y-direction can be obtained by differentiating those polynomials successively. We also obtained the drop velocity and acceleration using the central difference formula of 2<sup>nd</sup> order. Figure 7 (A) shows how well the ridge regression polynomial fits the data of the drop centroid displacement in the x-direction at  $We = 19.8$ . Figures 7 (B) and 8 compare the outcomes of the two approaches used to calculate the drop velocity and acceleration at  $We = 19.8$ .

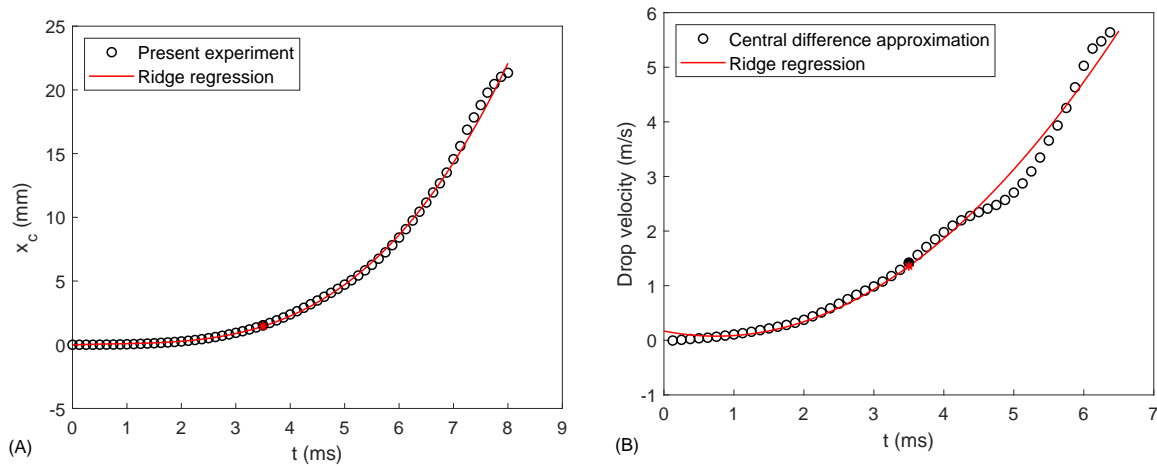


**Figure 7.** (A) Polynomial fit to the data of drop centroid displacement in the x-direction ( $x_c$ ) using ridge regression at  $We = 19.8$ , and (B) drop velocity calculated using the same displacement data. The drop velocity is calculated by (1) using central difference formula of 2<sup>nd</sup> order, and (2) differentiating the polynomial from Fig. 7 (A) at  $We = 19.8$  (the filled circle and asterisk markers in both the plots represent the displacement of the drop centroid and the drop velocity at the initiation time).

The drop velocity calculated using the central difference formula matches well with the one calculated by differentiating the polynomial which was obtained using the ridge regression (Fig. 7 (B)). A similar observation can be made for the drop acceleration (except for the earlier times) until the initiation time (Fig. 8). We see fluctuations in the drop acceleration values before the initiation time whose magnitude increases after the initiation time. The reason could be the implementation of numerical differentiation which amplifies small fluctuations/errors in empirical data [2] (in such cases, it is recommended to fit a smooth, differentiable function to the data using regression analysis [2] which we did). Another probable reason, as mentioned before, behind the large fluctuations in the drop acceleration values after the initiation time could be the centroid of the drop not being the actual center of mass. After the initiation time, structures like toroidal rim, bag, stamen and core drop starts appearing (Fig. 3). The quantity of mass in these structures is unknown. Hence, the drop velocity and acceleration values after the initiation time may not be reliable [4].

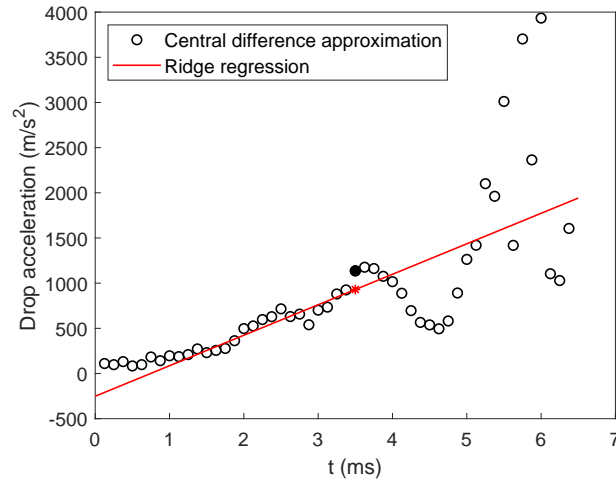


**Figure 8.** Drop acceleration calculated using the data for drop centroid displacement in the x-direction at  $We = 19.8$ . The drop acceleration is calculated by (1) using central difference formula of 2<sup>nd</sup> order, and (2) differentiating the polynomial from Fig. 7 (A) twice (the filled circle and asterisk markers represent the acceleration of the drop at the initiation time).

Once the velocity, acceleration and cross-stream length of the drop are known, its coefficient of drag ( $C_d$ ) can be calculated using the following expression [16],

$$C_d = \frac{m_d a_d}{\frac{1}{2} \rho_a V_{slip}^2 A_f}, \quad (6)$$

where  $m_d$  and  $a_d$  are the mass and acceleration of the drop respectively,  $V_{slip}$  is the relative velocity between the drop and the gas, and  $A_f$  is the frontal area of the drop facing the gas flow.  $V_{slip}$  is expressed as  $V_{slip} = |V_d - V_{gas}|$ , where  $V_d$  and  $V_{gas}$  are the drop and gas velocities, respectively.  $V_d$  represents the drop velocity in the x-direction in the expression for  $V_{slip}$ . For calculating  $A_f$ , the cross-stream length of the drop ( $2R$ ) is used.

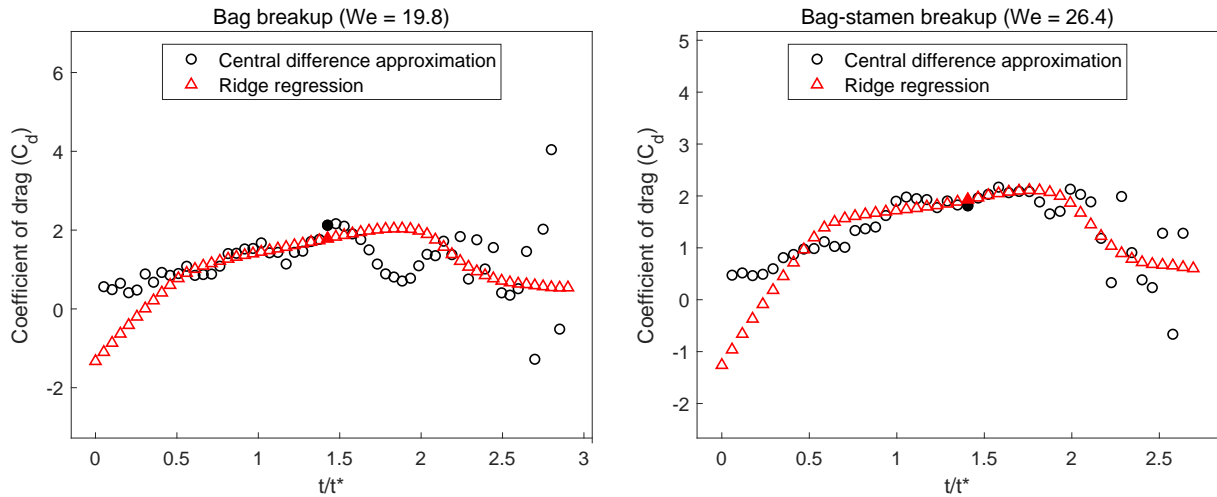


**Figure 9.** Variation of coefficient of drag ( $C_d$ ) with  $t/t^*$  in at  $We = 19.8$  and  $We = 26.4$  the present experiments (the filled markers show the coefficient of drag ( $C_d$ ) at the initiation time).

Figure 9 shows the variation of  $C_d$  with  $t/t^*$  at  $We = 19.8$  and  $We = 26.4$  in the present experiments. The  $C_d$  values calculated using the drop velocity and acceleration obtained through ridge regression and central difference approximation are termed as  $C_{d,RR}$  and  $C_{d,CDA}$ , respectively. We see fluctuations in the  $C_{d,CDA}$  values, which could be because of the fluctuations in the drop velocity and acceleration values (Figs. 7 and 8). Such fluctuations in the  $C_d$  values are observed in the literature also [3, 4, 7, 11]. The  $C_{d,CDA}$  values are close to 0.5 at the earlier times as observed in [3, 7, 11]. Near the first rupture time, unrealistic values of  $C_{d,CDA}$  are observed. As mentioned before, the drop velocity, acceleration, and hence, the  $C_d$  values may not be reliable after the initiation time as the drop centroid is not the true representation of its center of mass.

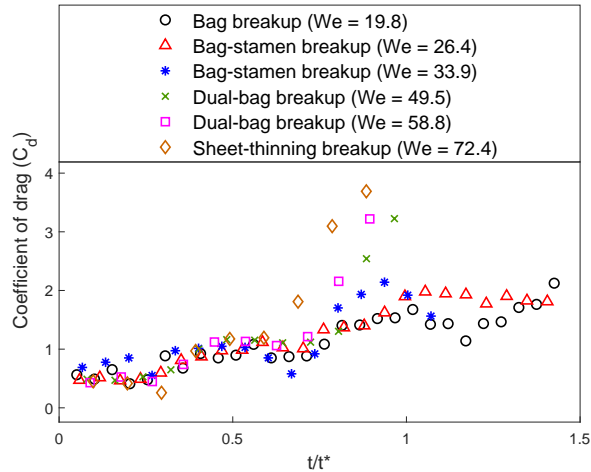


**Figure 10.** Variation of coefficient of drag ( $C_d$ ) with  $t/t^*$  till the initiation time in the present experiments.

The  $C_{d,RR}$  values at  $We = 19.8$  and  $We = 26.4$ , in the earlier times, are negative. It is because of the nature of the polynomial fit to the displacement data, which resulted in negative acceleration values as are seen in Fig. 8. At the later times, at  $We = 19.8$  and  $We = 26.4$ ,  $C_{d,RR}$  seems to be averaging  $C_{d,CDA}$ . Also, at the initiation time, the match between the values of  $C_{d,RR}$  and  $C_{d,CDA}$  is quite satisfactory. At higher Weber numbers ( $We = 49.5$ ,  $We = 58.8$ , and  $We = 72.4$ ), we did not observe a good agreement between the values of  $C_{d,RR}$  and  $C_{d,CDA}$ . The  $C_{d,CDA}$  values seem more realistic [3, 4] compared to those of  $C_{d,RR}$ .

Figure 10 shows the variation of  $C_{d,CDA}$  values with  $t/t^*$  till the initiation times at six Weber numbers from the present experiments. At  $We = 19.8, 26.4, 33.9$  (where bag and bag-stamen breakup were observed), the values of  $C_{d,CDA}$ , more or less, follow the same trend. The maximum  $C_{d,CDA}$  values are close to 2. However, at  $We = 49.5, 58.8, 72.4$  (where dual-bag and sheet-thinning breakup were observed), we see an increase in the  $C_{d,CDA}$  values towards the end of the initiation time. It could be happening because of (1) the high acceleration of the drops at higher Weber numbers, and (2)  $C_d$  being the function of shapes the drop attains over the initiation time (the shape of the drop at the initiation time in bag and bag-stamen breakup (Fig. 3 (A - c, B - c, C - c)) is significantly different from that in dual-bag and sheet-thinning breakup (Fig. 3 (D - b, E - b))).

Flock *et al.* [4] calculated the drop velocity and acceleration from the drop centroid displacement data using central difference approximation. They performed experiments with ethanol at  $We = 13$  ( $Oh = 0.0059$ ,  $Re = 1500$ ) and  $We = 32$  ( $Oh = 0.0059$ ,  $Re = 2500$ ), and observed bag breakup and sheet-thinning breakup modes, respectively. We observed the same breakup modes in our experiments at  $We = 19.8$  and  $We = 72.4$ , respectively. At  $We = 33.9$  (which is close to  $We = 32$  from [4]) in the present experiments, we observed bag-stamen breakup. This gives us an opportunity to compare  $C_{d,CDA}$  values when (1) Weber numbers are close to each other, but breakup modes are different, and (2) breakup modes are the same, but Weber numbers are different. We consider only  $We$  while making the comparison because: (1)  $Oh < 0.1$  in both the studies. As mentioned in Section 'Introduction',  $We$  is the most influential parameter when  $Oh < 0.1$  as viscous effects can be neglected [6], (2) As long as the  $We$  is held constant, the variation in  $Re$  does not play a significant role in breakup behaviour of the drop [10].

Figures 11 and 12 compare temporal evolution of coefficients of drag from our study and [4] till the initiation times. As can be seen in Fig. 11 (A), the  $C_{d,CDA}$  values from [4] at  $We = 32$  (sheet-thinning breakup) are always larger than those from the present experiments at  $We = 33.9$  (bag-stamen breakup). There is hardly any overlap in the data from [4] and our experiments. However, when the breakup modes are the same but Weber numbers are different (Fig. 11 (B)), the maximum values of  $C_{d,CDA}$  attained at both the Weber numbers are close to each other. This hints that the coefficient of drag ( $C_d$ ) could be a strong function of breakup mode rather than Weber number. The fact that the coefficient of drag ( $C_d$ ) is a function of the shape of the object supports the above statement because the shapes, drops of different liquids attain during their deformation in the same breakup mode, are similar. Ideally, there should have been a reasonably good match between  $C_{d,CDA}$  values in Fig. 11 (B) if the coefficient of drag ( $C_d$ ) is a strong function of breakup mode. The reason behind the mismatch could be the use of different experimental setups and conditions as there are many uncertain factors such as turbulence effects and measurement errors [17]. The best way to confirm the dependence of coefficient of drag ( $C_d$ ) on a breakup mode and the Weber number is to carry out experiments on two different liquids using the same experimental setup. Figure 12 shows a comparison between  $C_{d,CDA}$  values at  $We = 13$  (from [4]) and  $We = 19.8$  (from the present experiments), where the bag breakup mode was observed. Again, we observe overlap in the data from [4] and our experiments even though the Weber numbers are different. This observation supports the hypothesis that the coefficient of drag could be a strong function of breakup mode than the Weber number.

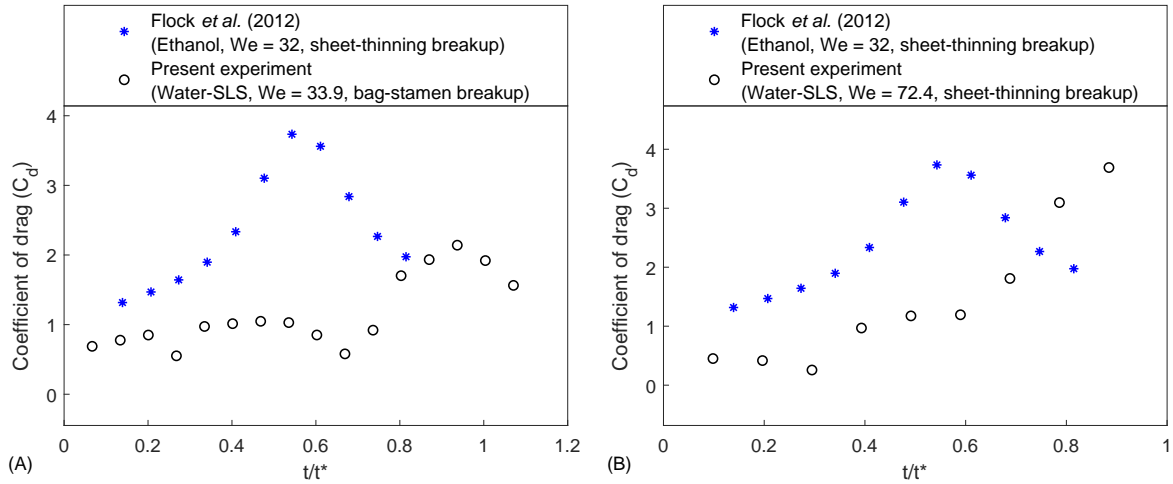


**Figure 11.** Comparison between the values of coefficients of drag ( $C_d$ ) from the present experiments and [4] at (A) nearly the same Weber numbers (but different breakup modes), and (B) different Weber numbers (but the same breakup modes). (Central difference approximation was used for calculating the drop velocity and acceleration.)

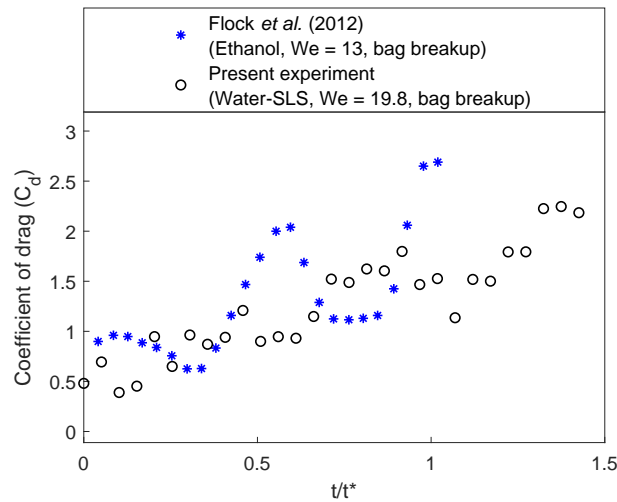


**Figure 12.** Comparison between the values of coefficients of drag ( $C_d$ ) from the present experiments and [4] at different Weber numbers (but the same breakup mode). (Central difference approximation was used for calculating the drop velocity and acceleration.)

## Conclusions

Breakup behaviour of a surfactant-laden drop was investigated in a cross-flow over a wide range of Weber numbers. The first rupture time and temporal evolution of stream-wise and cross-stream lengths of the drop until the first rupture time are functions of Weber number. At low Weber numbers (where bag and bag-stamen breakup were observed), the polynomial, fit to the displacement data of the drop centroid using the ridge regression, can be used to predict the drop velocity and acceleration reasonably close to the ones predicted by a central difference approximation, till the initiation time. A similar conclusion can be made for the prediction of coefficient of drag ( $C_d$ ) values too. However, in the initial stage of the drop deformation (at low Weber numbers), the prediction of the drop acceleration and coefficient of drag ( $C_d$ ) using the ridge regression is unrealistic. Till the initiation time, it appears that the coefficient of drag ( $C_d$ ) is a strong function of the breakup mode than Weber number.

## Nomenclature

$We$	Weber number
$Oh$	Ohnesorge number
$\sigma$	surface tension [N/m]
$\mu_l$	liquid viscosity [kg/m·s]
$\rho_l$	liquid density [kg/m <sup>3</sup> ]
$\rho_a$	gas density [kg/m <sup>3</sup> ]
$U$	initial relative velocity between the drop and flow-field
$d_0$	undeformed drop diameter

$SLS$	sodium lauryl sulfate
$CMC$	critical micelle concentration
$R$	half the cross-stream length of the drop
$L$	stream-wise length of the drop
$\lambda$	tuning parameter
$RSS$	sum of squared residuals
$\beta$	regression coefficient
$C_d$	coefficient of drag
$m_d$	mass of the drop
$a_d$	acceleration of the drop
$V_{slip}$	relative velocity between the drop and the gas
$A_f$	frontal area of the drop

## References

- [1] Cao, X. K., Sun, Z. G., Li, W. F., Liu, H. F., and Yu, Z. H. (2007). *Physics of Fluids*, 19(5).
- [2] Chapra, S. C. and Canale, R. P. (2010). *Numerical methods for engineers*. McGraw-Hill Higher Education, Boston, 6th edition.
- [3] Chou, W.-H. and Faeth, G. (1998). *International Journal of Multiphase Flow*, 24(6):889 – 912.
- [4] Flock, A. K., Guildenbecher, D. R., Chen, J., Sojka, P. E., and Bauer, H. J. (2012). *International Journal of Multiphase Flow*, 47:37–49.
- [5] Guildenbecher, D. R., López-Rivera, C., and Sojka, P. E. (2009). *Experiments in Fluids*, 46(3):371–402.
- [6] Hsiang, L.-P. and Faeth, G. (1992). *International Journal of Multiphase Flow*, 18(5):635 – 652.
- [7] Jain, M., Prakash, R. S., Tomar, G., and Ravikrishna, R. V. (2015). *Proceedings of the Royal Society A: Mathematical, Physical and Engineering Sciences*, 471(2177):20140930–20140930.
- [8] James, G., Witten, D., Hastie, T., and Tibshirani, R., editors (2013). *An introduction to statistical learning: with applications in R*. Number 103 in Springer texts in statistics. Springer, New York.
- [9] Karapetsas, G., Craster, R. V., and Matar, O. K. (2011). *Journal of Fluid Mechanics*, 670:5–37.
- [10] Lee, C. H. and Reitz, R. D. (2000). *International journal of multiphase flow*, 26(2):229–244.
- [11] Liu, A. B., Mather, D., and Reitz, R. D. (1993). In *SAE Technical Paper*. SAE International.
- [12] Nicholls, J. A. and Ranger, A. A. (1969). *AIAA Journal*, 7(2):285–290.
- [13] Pilch, M. and Erdman, C. A. (1987). *International Journal of Multiphase Flow*, 13(6):741–757.
- [14] Strotos, G., Malgarinos, I., Nikolopoulos, N., and Gavaises, M. (2016). *International Journal of Multiphase Flow*, 85:96–109.
- [15] Turro, N. J. and Yekta, A. (1978). *Journal of the American Chemical Society*, 100(18):5951–5952.
- [16] Vargas, M., Sor, S., and García Magariño, A. (2013). American Institute of Aeronautics and Astronautics.
- [17] Wang, C., Chang, S., Wu, H., Ding, L., and Thompson, J. (2015). *Atomization and Sprays*, 25(10):857–869.
- [18] Zhao, H., Zhang, W.-B., Xu, J.-L., Li, W.-F., and Liu, H.-F. (2016). *Physics of Fluids*, 28(5):054102.
- [19] Zhao, H., Zhang, W.-B., Xu, J.-L., Li, W.-F., and Liu, H.-F. (2017). *Experiments in Fluids*, 58(3).